\$ 5 EVIER

Contents lists available at ScienceDirect

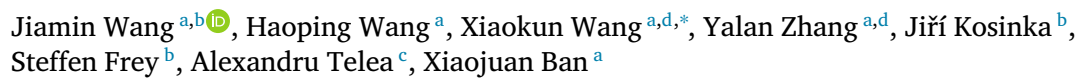
# Computers & Graphics

journal homepage: www.elsevier.com/locate/cag



Special Section on AniNex 2025

# Peridynamics-based simulation of viscoelastic solids and granular materials<sup>☆</sup>



- <sup>a</sup> School of Intelligence Science and Technology, University of Science and Technology Beijing, Beijing, China
- <sup>b</sup> Bernoulli Institute, University of Groningen, Groningen, The Netherlands
- <sup>c</sup> Faculty of Science, Utrecht University, Utrecht, The Netherlands
- d Shunde Innovation School, University of Science and Technology Beijing, Foshan, China

#### ARTICLE INFO

# Keywords: Peridynamics Viscoelastic simulation Granular materials Multi-material coupling

#### ABSTRACT

Viscoelastic solids and granular materials have been extensively studied in Classical Continuum Mechanics (CCM). However, CCM faces inherent limitations when dealing with discontinuity problems. Peridynamics, as a non-local continuum theory, provides a novel approach for simulating complex material behavior. We propose a unified viscoelasto-plastic simulation framework based on State-Based Peridynamics (SBPD) which derives a time-dependent unified force density expression through the introduction of the Prony model. Within SBPD, we integrate various yield criteria and mapping strategies to support granular flow simulation, and dynamically adjust material stiffness according to local density. Additionally, we construct a multi-material coupling system incorporating viscoelastic materials, granular flows, and rigid bodies, enhancing computational stability while expanding the diversity of simulation scenarios. Experiments show that our method can effectively simulate relaxation, creep, and hysteresis behaviors of viscoelastic solids, as well as flow and accumulation phenomena of granular materials, all of which are very challenging to simulate with earlier methods. Furthermore, our method allows flexible parameter adjustment to meet various simulation requirements.

#### 1. Introduction

Viscoelastic solids and granular materials are ubiquitous in our daily lives and industrial production. From kneading dough and biological soft tissues to natural disasters like avalanches and mudflows, these materials demonstrate complex dynamic characteristics. Accurate simulation of these behaviors is of great significance to fields such as materials science, geotechnical engineering, biomedical simulation, and – last but not least – computer graphics.

Viscoelastic solids have time-dependent characteristics including stress relaxation, creep, and hysteresis. For large deformations, memory effects and nonlinearities further complicate the simulation. Granular materials consist of a large number of discrete particles and can exhibit both the shear resistance of solids and the deformability of fluids. Recent advances in computational and physical modeling techniques have made the accurate simulation of viscoelastic and granular materials an active area of research in both computer graphics and computational physics

Early simulation methods used mesh-based discretization strategies such as the Finite Element Method (FEM) [1] and described the time-dependent behavior of viscoelastic materials by generalized Maxwell or

Kelvin–Voigt models. While widely used in structural mechanics, when handling fractures, separations, and large deformations, such models encounter complex challenges when topology changes and meshes need reconstruction. Mesh-free methods such as Smoothed Particle Hydrodynamics (SPH), the Material Point Method (MPM), and Position-Based Dynamics (PBD) compute physical interactions through particle-based interactions and show clear advantages in handling fracture, large deformation, and free surface flows. They can model a wide range of natural phenomena and materials such as muscle [2], sand [3,4], snow [5,6], and multi-material mixtures [7,8].

However, most existing mesh-free methods still rely on CCM with foundations in partial differential equations (PDEs). PDEs are not applicable at *discontinuities*, e.g., cracks and interface slippage; additional techniques are needed to capture such phenomena. The Peridynamics method [9] replaces differential with integral equations to naturally handle material discontinuities. State-Based Peridynamics (SBPD) [10] further expanded the range of constitutive models by introducing the *deformation state* and *force state* concepts. Recent developments have showcased the versatility of the Peridynamics method in simulating diverse material behaviors, such as hyperelastic thin membranes with

E-mail address: wangxiaokun@ustb.edu.cn (X. Wang).

 $<sup>\</sup>stackrel{\dot{}}{lpha}$  This article is part of a Special issue entitled: 'AniNex2025' published in Computers & Graphics.

<sup>\*</sup> Corresponding author.

complex contact interactions [11], and fracture in elastoplastic materials [12]. While some viscoelastic and elastoplastic models have been developed within the Peridynamics framework, the potential for granular flow simulation and unified coupling with viscoelastic bodies remains underexplored.

In this paper, we propose a unified viscoelasto-plastic simulation framework based on SBPD that supports both the time-dependent behavior of viscoelastic solids and the yield-driven flow dynamics of granular materials, with the following key contributions:

- We introduce the Prony model to an SBPD-based framework to derive time-dependent force density expressions, accurately capturing *relaxation*, *creep*, and *hysteresis*.
- We integrate various yield criteria and plastic mapping strategies within SBPD, combine them with dynamic and static friction forces and density-based stiffness adjustments, and achieve realistic granular flows.
- We create a multi-material coupling system supporting interactions between viscoelastic solids, granular materials, and rigid bodies. This improves computational stability and significantly enriches the diversity of simulation scenarios.

#### 2. Related work

#### 2.1. Viscoelastic simulation

Viscoelastic materials under external loads exhibit both equilibrium elastic responses and non-equilibrium viscous characteristics.

Terzopoulos and Fleischer [13,14] pioneered the use of elastic models into computer graphics and expanded them into three typical non-elastic behavior simulations including viscoelasticity, plasticity, and fracture. Müller et al. [15] introduced SPH into computer graphics, greatly promoting the application of meshless methods in deformable body simulation. Takahashi et al. [16] proposed an implicit SPH method for stable simulation of highly viscous fluids. Peer et al. [17], by extracting rotation from the SPH deformation gradient, improved the efficiency of elastic solid simulation nearly hundredfold. The MPM [5] is a particle-grid hybrid method initially introduced to graphics primarily for snow simulation, and subsequently extended to handle many materials and phase transitions [18]. Yue et al. [19] used MPM to simulate shear-dependent dense foams. Current research on viscoelasticity in computer graphics primarily focuses on viscoelastic fluids and much less on viscoelastic solids. Fang et al. [20] proposed a predictor-corrector algorithm that achieves viscoelastic and elastoplastic solid simulation under large deformation conditions.

Peridynamics has attracted increasing interest due to its advantages in handling material failure problems such as cutting and crack propagation [21]. Yet, developing systematic viscoelastic models within a peridynamics framework remains limited. Madenci et al. [22] proposed a viscoelastic constitutive model based on ordinary state-based peridynamics, capturing material relaxation characteristics under mechanical and thermal loads. Ozdemir et al. [23] further modeled crack propagation in films based on this approach. Our method differs from theirs; although also based on the Prony model, we have derived a unified force density expression by combining it with a corotational elastic energy model.

# 2.2. Granular flow simulation

Continuum methods have been widely used in graphics to simulate granular materials. Zhu and Bridson [24] simulated sand through an improved PIC fluid solver. Narain et al. [25] made key improvements to this method, effectively eliminating cohesive artifacts related to incompressibility, significantly enhancing simulation quality. Lenaerts and Dutre [26] implemented coupling interactions between water and sand based on the SPH method. Daviet and Bertails-Descoubes [27]

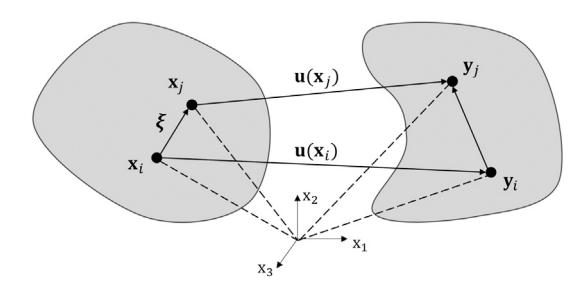


Fig. 1. Deformation state mapping.

developed a MPM-based granular material model that behaves like a solid due to internal friction, representing granular matter as a viscoplastic fluid combining the Drucker–Prager yield criterion and unilateral compressibility constraints. Tampubolon et al. [7] proposed a multi-phase MPM simulation of sand–water mixtures, handling fluid permeation and interaction in sand via porous media theory.

Compared to SPH and MPM methods, Peridynamics-based simulation of granular materials is an emerging research direction with great potential. In structural mechanics, Peridynamics is commonly used to simulate the fracture of geotechnical materials under loading [28]. However, current research on Peridynamics for simulating granular flows remains relatively limited, particularly lacking a framework that unifies viscoelastic response with granular plastic flow.

#### 3. SBPD theory

State-based Peridynamics (SBPD) is a reformulation of continuum mechanics. Unlike bond-based peridynamics, which models particle interactions as springs, SBPD defines interactions through the relation between a particle and its neighborhood. This allows for asymmetric forces and the modeling of more complex material behavior.

Let  $\mathcal H$  denote a spherical neighborhood of radius r and center  $\mathbf x_i$ . Let  $\mathcal L_m$  denote the space of order-m tensors. An order-m state is a mapping  $\mathbf A\langle \xi \rangle : \mathcal H \to \mathcal L_m$ , where  $\xi = \mathbf x_j - \mathbf x_i, \xi \in \mathcal H$  is the so-called bond vector between particle  $\mathbf x_i$  and its neighbor  $\mathbf x_j$ . Let  $\mathbf y = \varphi(\mathbf x)$  denote a deformation under a motion  $\varphi$ . The corresponding reference and deformation vector states (see Fig. 1) are defined as  $\mathbf X\langle \xi \rangle = \mathbf x_j - \mathbf x_i$  and  $\mathbf Y\langle \xi \rangle = \mathbf y_j - \mathbf y_i$ .

Classical continuum mechanics defines the deformation gradient as  $F(x)=\partial y/\partial x.$  Yet, this partial derivative does not exist at discontinuities. To overcome this, Peridynamics approximates F using a least-squares minimization over  $\mathcal H$  as  $F=(Y*X)(X*X)^{-1}$  with the generalized tensor product defined by

$$\mathbf{A} * \mathbf{B} = \int_{\mathcal{H}} w(\xi) \, \mathbf{A} \langle \xi \rangle \otimes \mathbf{B} \langle \xi \rangle \, d\xi, \tag{1}$$

where  $w(\xi)$  is a weight function and  $\otimes$  denotes the dyadic product. In our implementation, we adopt the Wendland  $C_2$  kernel for  $w(\xi)$  due to its compact support and  $C^2$  continuity, and we set the horizon radius r to be twice the particle size, which provides stable and consistent neighborhood interactions.

The motion of particle i is governed by the balance of linear momentum in integral form

$$\rho_i \mathbf{a}_i = \int_{\mathcal{U}} \left( \mathbf{T}_i \langle \xi \rangle - \mathbf{T}_j \langle -\xi \rangle \right) d\xi + \mathbf{g}, \tag{2}$$

where  $\rho_i$  is the density of particle i,  $\mathbf{a}_i$  is its acceleration,  $\mathbf{g}$  is the external body force, and the state function  $\mathbf{T}$  models internal forces.

### 4. Viscoelastic constitutive model

We extend the classical elastic SBPD framework to incorporate viscoelastic behavior using a Prony-series-based energy model. Our approach captures time-dependent effects such as creep, relaxation, and hysteresis through control parameters. We implement our approach in a discrete numerical form that is compatible with particle-based simulations.

The Prony model [29] is a widely used linear viscoelastic constitutive model which models the material's stress response  $\sigma$  as a sum of exponentially decaying functions via

$$\sigma(t) = E_{\infty} \cdot \varepsilon(t) + \sum_{k=1}^{N} E_k \cdot e^{-t/\theta_k} \cdot \varepsilon(t), \tag{3}$$

where  $\varepsilon$  is strain, N is the approximation order,  $E_{\infty}$  is the steady-state modulus, and  $E_k$  and  $\theta_k$  are the relaxation modulus and relaxation time of the kth mode, respectively.

To implement this model numerically, we discretize time and introduce variables  $q_{\nu}$  to capture the memory effect associated with each mode. These variables are updated over time as

$$q_{\nu}^{n+1} = \alpha_{\nu} \cdot q_{\nu}^{n} + (1 - \alpha_{\nu}) \cdot \varepsilon^{n+1}, \tag{4}$$

where  $\alpha_k = e^{-\Delta t/\theta_k}$ . Each  $q_k$  term gives the contribution of a specific relaxation mode and decays exponentially over time. This yields the stress update rule

$$\sigma^{n+1} = E_{\infty} \cdot \varepsilon^{n+1} + \sum_{k=1}^{N} E_k \cdot \left( \varepsilon^{n+1} - q_k^{n+1} \right). \tag{5}$$

Similar to the projected Peridynamics elastic model of by He et al. [30], we use a linear co-rotational elastic energy model to simulate the hyperelastic body and decompose it into a deviatoric part  $\mathcal{W}^{dev}$  and an isotropic part  $\mathcal{W}^{iso}$ 

$$\Psi = \int_{\mathcal{H}} w\langle \xi \rangle \left( \mu \, \mathcal{W}^{\text{dev}} \langle \xi \rangle + \frac{\lambda}{2} \, \mathcal{W}^{\text{iso}} \langle \xi \rangle \right) d\xi, \tag{6}$$

where  $\mu$  and  $\lambda$  are the first and the second Lamé parameters, respectively. Assuming that all particles in  ${\cal H}$  share the same deformation gradient F, the ideal deformation tensor state can be expressed as  $\hat{\mathbf{Y}} = \mathbf{F}\boldsymbol{\xi}$ .  $\mathcal{W}^{\text{dev}}$  is the energy of shear deformation and  $\mathcal{W}^{\text{iso}}$  is the energy of volume deformation, which are defined as

$$\mathcal{W}^{\text{dev}} = (|\hat{\mathbf{Y}}|/|\mathbf{X}| - 1)^2,$$
  

$$\mathcal{W}^{\text{iso}} = (|\mathbf{Y}|/|\mathbf{X}| - 1)^2.$$
(7)

When the horizon  $\mathcal{H}$  is small and the deformation field is smooth,  $\hat{\mathbf{Y}} \approx \mathbf{Y}$ .

For each relaxation mode, we can now express the time evolution of the energy via our internal history variables as

$$\begin{split} & \boldsymbol{\mathcal{Y}}_{i,j}^{\text{dev}} = \boldsymbol{\mu}_{\infty} \boldsymbol{\mathcal{W}}_{i,j}^{\text{dev}} + \sum_{k=1}^{N} \boldsymbol{\mu}_{k} \left( \boldsymbol{\mathcal{W}}_{i,j}^{\text{dev}} - \boldsymbol{q}_{i,j}^{\text{dev},k} \right), \\ & \boldsymbol{\mathcal{Y}}_{i,j}^{\text{iso}} = \frac{\lambda_{\infty}}{2} \boldsymbol{\mathcal{W}}_{i,j}^{\text{iso}} + \sum_{k=1}^{N} \frac{\lambda_{k}}{2} \left( \boldsymbol{\mathcal{W}}_{i,j}^{\text{iso}} - \boldsymbol{q}_{i,j}^{\text{iso},k} \right), \end{split} \tag{8}$$

where, following (4), we have that

$$q_{i,j}^{\text{dev},k,n+1} = \alpha_k q_{i,j}^{\text{dev},k,n} + (1 - \alpha_k) \mathcal{W}_{i,j}^{\text{dev},n},$$

$$q_{i,j}^{\text{iso},k,n+1} = \alpha_k q_{i,j}^{\text{iso},k,n} + (1 - \alpha_k) \mathcal{W}_{i,j}^{\text{iso},n}.$$
(9)

The deviatoric force density is expressed as

$$\begin{split} \mathbf{T}_{ij}^{\text{dev}} &= \frac{2w(\boldsymbol{\xi})\gamma^{\text{dev}}}{|\mathbf{X}|^2} (|\mathbf{Y}| - |\mathbf{X}|) \text{dir}(\hat{\mathbf{Y}}), \text{ with} \\ \gamma^{\text{dev}} &= \mu_{\infty} + \sum_k \mu_k \left( 1 - \frac{q_{i,j}^{\text{dev},k}}{\mathcal{W}_{i,j}^{\text{dev}}} \right). \end{split} \tag{10}$$

Similarly, the isochoric force density is given by

$$\begin{split} \mathbf{T}_{ij}^{\mathrm{iso}} &= \frac{w(\xi)\gamma^{\mathrm{iso}}}{|\mathbf{X}|^2} (|\mathbf{Y}| - |\mathbf{X}|) \mathrm{dir}(\mathbf{Y}), \text{ with} \\ \gamma^{\mathrm{iso}} &= \lambda_{\infty} + \sum_{k} \lambda_{k} \left( 1 - \frac{q_{i,j}^{\mathrm{iso},k}}{\mathcal{W}_{i,j}^{\mathrm{iso}}} \right). \end{split} \tag{11}$$

In the above,  $\gamma$  is the effective modulus, *i.e.*, the effective stiffness of the deviatoric and isotropic components of the material at the current moment t. Using (10) and (11), we get the total force density  $T_{ij}$  =  $\mathbf{T}_{ij}^{\text{dev}} + \mathbf{T}_{ij}^{\text{iso}}$ . Finally, we derive the discrete form of the equation of motion

$$\rho_i \mathbf{a}_i = h^2 \sum_{j \in \mathcal{H}} \left( \mathbf{T}_{ij}(\xi) - \mathbf{T}_{ji}(-\xi) \right) V_j. \tag{12}$$

#### 5. Granular material simulation

Granular materials such as sand and snow often exhibit discrete elastoplastic behavior in the framework of continuum mechanics. We propose a peridynamics-based simulation method for granular flows under different yield criteria. We adopt the unified yield criterion proposed by Tu et al. [18] and implement three projection strategies for plastic mapping. Additionally, we dynamically update the Lamé parameters based on particle density to correct particle positions and enhance simulation stability.

#### 5.1. Yield modeling for different materials

When the internal stress state of a particle reaches the yield condition, irreversible plastic deformation occurs. We employ the Drucker-Prager yield criterion to define the yield surface as

$$y_{dp} = C_f \operatorname{tr}(\tau) + \sqrt{J_2} - C_c, \tag{13}$$

where  $\tau$  is the Kirchhoff stress tensor,  $s = \text{dev}(\tau)$  is its deviatoric part, and  $tr(\cdot)$  denotes the trace operator. The quantity  $J_2 = \frac{1}{2} s$ : s is the second invariant of s, and  $\sqrt{J_2}$  is used as the equivalent shear stress.

Here,  $C_f$  is a friction-related parameter that controls the slope of the yield surface, while  $C_c$  represents the cohesion of the material and determines the intercept of the yield surface. The ratio  $\tau_{\rm max}$  $C_c/C_f$  defines the apex stress of the yield surface, corresponding to the maximum hydrostatic stress beyond which shear deformation no longer contributes to yielding. The effects of these parameters on the yield surface are illustrated in Fig. 2.

#### 5.2. Plasticity mapping strategy

We simulate plastic deformation of granular materials such as sand or snow by implementing a plasticity mapping strategy within the SBPD framework. We use a classical 'return mapping' algorithm where plasticity is evolved by an elastic predictor step followed by a plastic corrector step: In the prediction step, plastic flow is temporarily ignored and stress and internal variables are updated elastically, yielding a trial deformation gradient  $\mathbf{F}^{tr}$ . If the yield surface is exceeded, we enter the plastic correction step and project stress back to the yield surface.

To incorporate plastic flow, we compute the elastic left Cauchy-Green deformation tensor as

$$\mathbf{b}^{tr} = \mathbf{F}^{tr} \mathbf{F}^{trT}. \tag{14}$$

Assuming a purely elastic response, the Kirchhoff stress tensor can be defined using a Neo-Hookean model as

$$\mathbf{s}^{tr} = \mu J_{tr}^{-2/d} \left( \mathbf{b}^{tr} - \frac{1}{d} \operatorname{tr}(\mathbf{b}^{tr}) \mathbf{I} \right),$$
  

$$\boldsymbol{\tau}^{tr} = \mathbf{s}^{tr} + \frac{\kappa}{2} (J_{tr}^2 - 1) \mathbf{I},$$
(15)

where  $J_{tr} = \det(\mathbf{F}^{tr})$ ,  $\mu$  and  $\kappa$  are the Lamé parameters, and d is the spatial dimension. The tensor  $\mathbf{s}^{tr}$  captures the shear response, while  $\boldsymbol{\tau}^{tr}$ includes both volumetric and deviatoric contributions.

Depending on the trial stress state relative to the yield surface, we distinguish three cases:

Case A (elastic region). If  $y_{dp}(\tau^{tr}) \leq 0$ , the stress lies inside the yield surface and the state remains elastic  $\mathbf{F}^{n+1} = \mathbf{F}^{tr}$ .

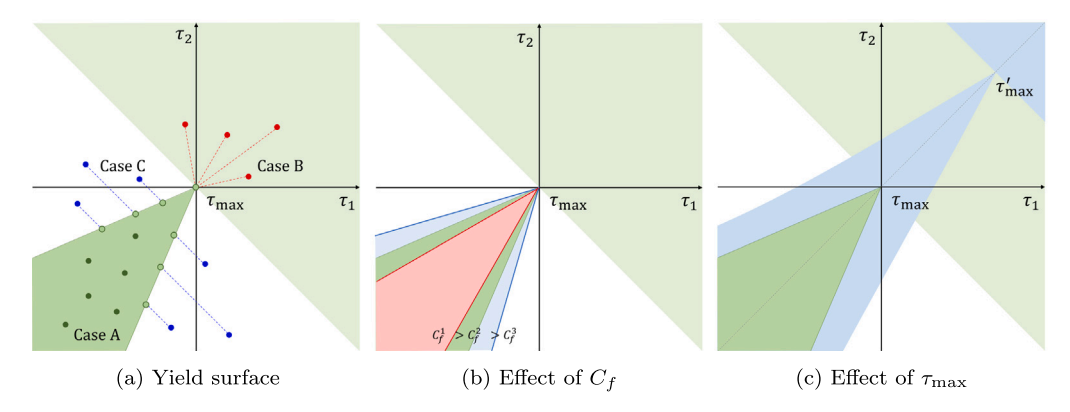


Fig. 2. Drucker–Prager yield surfaces and mapping mechanisms. (a) Illustration of the three projection cases on the Drucker–Prager yield surface. (b) Effect of the friction coefficient  $C_f$  on the yield cone angle. (c) Effect of the apex stress  $\tau_{\max}$ , which controls the position of the cone tip. A larger  $\tau'_{\max}$  (blue region) corresponds to higher cohesion  $C_c$ .

Case B (apex projection). If  ${\rm tr}(\tau^{tr})>\tau_{\rm max}$ , the stress reaches the apex of the yield surface. We then perform an isotropic correction

$$J^{n+1} = \sqrt{\frac{2}{d\kappa}} \tau_{\text{max}} + 1,$$

$$\Sigma^{n+1} = (J^{n+1})^{1/d} \cdot \mathbf{I}.$$
(16)

and reconstruct

$$\mathbf{F}^{n+1} = \mathbf{U} \boldsymbol{\Sigma}^{n+1} \mathbf{V}^T. \tag{17}$$

where U and V are obtained from the singular value decomposition of  $\mathbf{F}^{tr}$ 

Case C (general yield projection). If  $y_{dp}(\tau^{tr}) > 0$  but the apex condition is not met, we project the deviatoric stress magnitude while preserving its direction

$$\|\mathbf{s}^{n+1}\| = \max\left(0, \|\mathbf{s}^{tr}\| - \mathbf{y}_{dp}(\boldsymbol{\tau}^{tr})\right),$$
  
$$\mathbf{s}^{n+1} = \|\mathbf{s}^{n+1}\| \cdot \frac{\mathbf{s}^{tr}}{\|\mathbf{s}^{tr}\|}.$$
 (18)

The updated Cauchy-Green tensor is reconstructed as

$$\mathbf{b}_{dev} = \frac{\mathbf{s}^{n+1}}{\mu J_{tr}^{-2/d}}, \qquad \mathbf{b}_{base} = \mathbf{b}_{dev} + \frac{1}{d} \operatorname{tr}(\mathbf{b}^{tr})\mathbf{I}.$$
 (19)

To ensure consistency of the volumetric response, we introduce a correction  $\beta$  in the principal basis such that

$$(b_0 + \beta)(b_1 + \beta)(b_2 + \beta) = J_{tr}^2, \tag{20}$$

where  $b_0, b_1, b_2$  are the eigenvalues of  $\mathbf{b}_{base}$ . The corrected tensor is

$$\mathbf{b}^{n+1} = \text{diag}(b_0 + \beta, b_1 + \beta, b_2 + \beta), \tag{21}$$

and the updated deformation gradient follows as

$$\mathbf{F}^{n+1} = \mathbf{U}\operatorname{diag}(\sqrt{\mathbf{b}^{n+1}})\mathbf{V}^{T}.$$
 (22)

#### 5.3. Dynamic adjustment of stiffness

In granular flow simulation, we no longer use fixed Lamé parameters, but instead update these adaptively based on local material compaction. Drawing from snow material handling methods in MPM [5], we estimate elastic response changes based on the particle's current compression density. We compute the local density as

$$\rho_i = \sum_i m_j W(\mathbf{x}_i - \mathbf{x}_j, h), \tag{23}$$

where W is a kernel function with support radius h. The local density reflects the current compression level of the material, and the rest density reads  $\rho_{0,i}^t = \rho_i^t \left| \det(\mathbf{F}_i^t) \right|$ .

Using the ratio of this rest density to the initial density, we dynamically adjust the current Lamé parameters as

$$\lambda_{i}^{t} = \frac{E\nu}{(1+\nu)(1-2\nu)} \exp\left(\xi \cdot \frac{\rho_{0,i}^{t} - \rho_{0}}{\rho_{0,i}^{t}}\right),$$

$$\mu_{i}^{t} = \frac{E}{2(1+\nu)} \exp\left(\xi \cdot \frac{\rho_{0,i}^{t} - \rho_{0}}{\rho_{0,i}^{t}}\right).$$
(24)

This can be seen as a compression rate driven exponential hardening rule, which effectively enhances the response stiffness of materials such as snow in compacted states.

#### 6. Boundary handling

In the overall coupling of viscoelastic materials, granular flow materials, and rigid body boundaries, *boundary collision* mechanisms strongly influence simulation stability and realism. We introduce a boundary handling method using Sparse Signed Distance Fields (SDF) which improves stability and physical fidelity.

We directly sample and store SDF information on each rigid boundary particle, where each particle maintains a signed distance value  $\phi$  and its gradient  $\nabla \phi$ , representing the shortest distance to the boundary and its direction, respectively. This design allows particle-to-particle collision detection and avoids repeated grid-based sampling. Collisions are triggered when the distance between particles is below a threshold  $\|\mathbf{x}_i - \mathbf{x}_i\| < r$ , or when  $|\phi| < r$  for boundary contact.

Upon collision, particles are displaced along the contact normal direction with penetration depth  $d=\min(|\phi_i|,|\phi_j|)$  and mass-based weighting. The contact normal is approximated by the gradient of the closer particle's SDF. For example, the position correction for particle i is given by:

$$\Delta \mathbf{x}_{i} = -\frac{w_{i}}{w_{i} + w_{j}} (d \cdot \mathbf{n}_{ij}),$$

$$\Delta \mathbf{x}_{j} = \frac{w_{j}}{w_{i} + w_{j}} (d \cdot \mathbf{n}_{ij}),$$
(25)

where  $w_i = 1/m_i$ .

To resolve sliding or sticking effects at boundaries, we introduce both dynamic and static friction models, as follows.

**Dynamic friction:** During particle-boundary contact, we compute the change in velocity due to collision  $\Delta \mathbf{v}_i = \mathbf{v}_i^{n+1} - \mathbf{v}_i^*$ , where  $\mathbf{v}_i^{n+1}$  is the post-collision velocity and  $\mathbf{v}_i^*$  is the elastic response velocity. We compute the tangential velocity as

$$\mathbf{v}_{it} = \mathbf{v}_i^{n+1} - \mathbf{n}v_{in}, \quad v_{in} = \mathbf{n} \cdot \mathbf{v}_i^{n+1}. \tag{26}$$

With  $\mathbf{j} = m_i \Delta \mathbf{v}_i$  the impulse, the friction constraint reads  $\|\mathbf{f}_t\| \le c_b \|\mathbf{j}\|$ .

 Table 1

 Simulation information for selected examples. P is the number of particles.

Exp.	P	$\Delta t$	FPS	$E_0$	ν
Fig. 4	80k	5 ms	68.67	$1 \times 10^{8}$	0.45
Fig. 5	195k	2 ms	27.20	$1 \times 10^{7}$	0.45
Fig. 6	30k	5 ms	102.48	$1 \times 10^{7}$	0.45
Fig. 7	348k	2 ms	13.19	$3 \times 10^{5}$	0.20
Fig. 8	95k	5 ms	17.06	$2 \times 10^{5}$	0.20
Fig. 9	167k	2 ms	7.56	$2 \times 10^{5}$	0.20
Fig. 10	151k	2 ms	8.80	$5 \times 10^7$ (elast.) 1 × 10 <sup>5</sup> (sand)	0.45 0.20

When the friction force can completely eliminate the tangential velocity, the velocity correction is simply  $\mathbf{v}_i^{n+1} = \mathbf{n}v_{in}$ . Otherwise we set

$$\mathbf{v}_{i}^{n+1} = \mathbf{v}_{i}^{*} - \frac{c_{b}}{m_{i}} \|\mathbf{j}\| \frac{\mathbf{v}_{it}}{\|\mathbf{v}_{it}\|}, \tag{27}$$

where  $c_h$  is the dynamic friction coefficient.

**Static friction:** To prevent persistent sliding near boundaries and simulate stacking behavior, we find stationary particles using a geometric criterion: If the motion of particle i satisfies

$$(\mathbf{y}_{i}^{t+1} - \mathbf{y}_{i}^{*}) \cdot (\mathbf{y}_{i}^{t} - \mathbf{y}_{i}^{*}) \ge \eta \|\mathbf{y}_{i}^{*} - \mathbf{y}_{i}^{t}\|^{2}, \tag{28}$$

we freeze its position, i.e., set  $\mathbf{y}_i^{t+1} = \mathbf{y}_i^t$ .  $\eta$  is the static friction coefficient, set to  $\eta = 0.8$  in our simulations.

#### 7. Implementation

We implemented our framework on an NVIDIA GeForce RTX 4090 GPU using the Taichi programming language for efficient parallel simulation. The overall simulation procedure is outlined in Algorithm 1, where we typically set the maximum number of iterations iter<sub>max</sub> to 6, and terminate early if the maximum iteration displacement falls below a predefined threshold  $\epsilon=10^{-4}$ . All visual results were rendered offline via Houdini. Detailed simulation performance information is given in Table 1.

# Algorithm 1 Elastomer-Sand Coupling Simulation Based on SBPD

- 1: **Input:**  $\mathbf{y}^t, \mathbf{v}^t$ , phase,  $\Delta t$ , iter<sub>max</sub>,  $E_0$ ,  $\nu$ ,  $E_\infty$ ,  $E_k$ ,  $\theta_k$ ,  $C_f$ ,  $C_c$ ,  $\eta$ ,  $\epsilon$ 2: Particle advection:  $\mathbf{y}^{t+1} \leftarrow \mathbf{y}^t + \mathbf{v}^t \Delta t$
- 3: **while** iteration < iter<sub>max</sub> and max  $(\|\Delta \mathbf{x}_i\|) > \epsilon$  **do**
- 4: // Elastic Phase:
- 5: Compute deformation gradient **F**
- 6: Compute force density T (Eq. (10), (11))
- 7: Compute displacement  $\Delta x$  (Eq. (12))
- 8: Update position:  $\mathbf{y}^{t+1} \leftarrow \mathbf{y}^{t+1} + \Delta \mathbf{x}$
- 9: // Sand Phase:
- 10: Compute deformation gradient  $\mathbf{F}$
- 11: Project F onto yield surface (Cases A/B/C)
- 12: Compute force density T
- 13: Compute displacement  $\Delta x$  (Eq. (12))
- 14: Update position:  $\mathbf{y}^{t+1} \leftarrow \mathbf{y}^{t+1} + \Delta \mathbf{x}$
- 15: end while
- 16: // Constraints and Collisions:
- 17: **while** iteration < iter<sub>max</sub> **do**
- 18: Apply self and inter-phase collision response (Eq. (25))
- 19: Apply boundary advection
- 20: end while
- 21: // Post-processing:
- 22: Update velocity:  $\mathbf{v}^{t+1} \leftarrow (\mathbf{y}^{t+1} \mathbf{y}^t) / \Delta t$
- 23: Apply static friction constraint
- 24: Apply dynamic friction constraint
- 25: Update neighbor list j
- 26: Update Lamé parameters (Eq. (24))

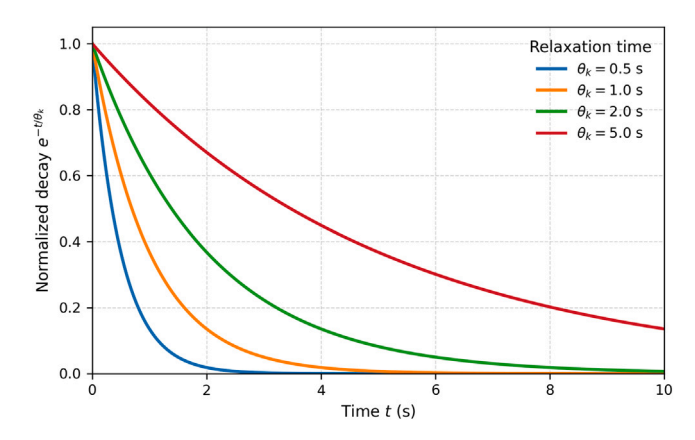


Fig. 3. Exponential decay of relaxation modes in the Prony model.

We validate our algorithm using a N=3 (rd) order Prony model. The total Young's modulus  $E_0$  gives the initial stiffness of the material, while the long-term modulus  $E_\infty$  characterizes its stiffness at infinite time. Each  $E_k$  denotes the relaxation modulus of the kth component, with  $\theta_k$  being the corresponding relaxation time. The material behavior is defined using the empirical relation:  $E_0=E_\infty+\sum_{k=1}^N E_k$ . The configuration of relaxation times at each order can be determined according to the empirical rules of exponential decay, as shown in Fig. 3.

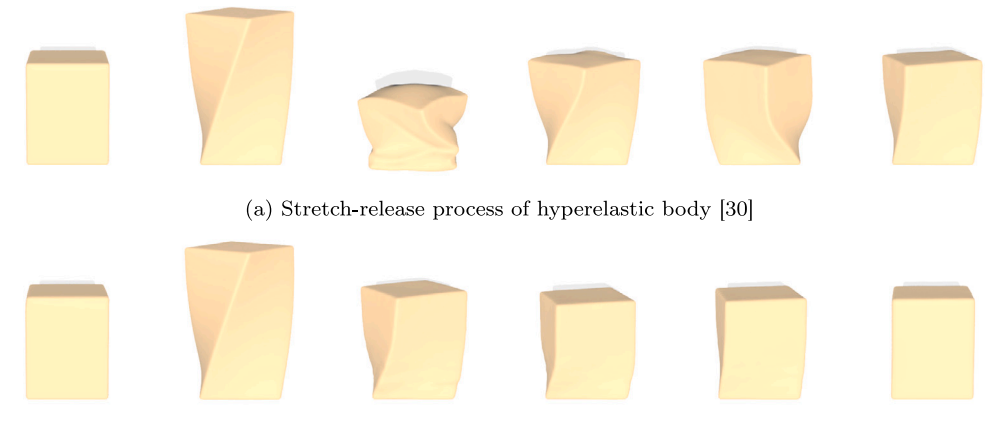
#### 8. Results and discussion

**Viscoelastic simulation:** Fig. 4 shows a rotational stretch-release experiment to compare the post-release recovery behavior of hyperelastic and viscoelastic materials. The hyperelastic model was configured with  $E_0=E_\infty$ , corresponding to a purely elastic response. Upon removal of the external load, the object rapidly rebounds and exhibits pronounced oscillations. For the viscoelastic model, we set  $E_\infty=0.4E_0$ ,  $E_k=[0.3,0.2,0.1]\cdot E_0$ , and  $\theta_k=[1.0,3.0,5.0]$ . After unloading, the material gradually returns to its original shape without oscillations (see the supplemental video).

We further illustrate the flexibility of our viscoelastic model by an "armadillo stretch-rest-unload" experiment with  $E_0 = 1 \times 10^7$  and v = 0.45. We compared three different viscoelastic material parameters:

- Purely elastic:  $E_{\infty} = E_0$ ;
- High viscosity:  $E_{\infty} = 0.3E_0$ ,  $E_k = [0.3, 0.2, 0.2] \cdot E_0$ ,  $\theta_k = [0.5, 2.0, 5.0]$ :
- Low viscosity:  $E_{\infty} = 0.5E_0$ ,  $E_k = [0.25, 0.15, 0.1] \cdot E_0$ ,  $\theta_k = [0.5, 2.0, 5.0]$ .

Fig. 5 shows the evolution of energy (in red) throughout the simulation and presents a quantitative analysis. During the stretching phase, the total energy of all three materials increases non-linearly due to the work done by external forces, consistent with the non-linear characteristics of stress–strain relationships. For hyperelastic material, the external work is entirely converted into elastic potential energy, whereas for viscoelastic materials, a portion of the energy is dissipated through viscous effects. In the constant-stretching phase, the energy of the elastic material remains unchanged, while the viscoelastic materials exhibit stress relaxation, demonstrating the physical plausibility of our model. In the relaxation phase, hyperelastic material released energy most rapidly and almost completely returned to its original state. Highly viscous materials release energy more slowly, showing significant hysteresis effects as part of the energy is converted to heat through viscous mechanisms. The energy release rate of the low-viscosity elastic



(b) Stretch-release process of viscoelastic body

Fig. 4. Comparison of recovery behavior during a rotational stretch-release experiment.

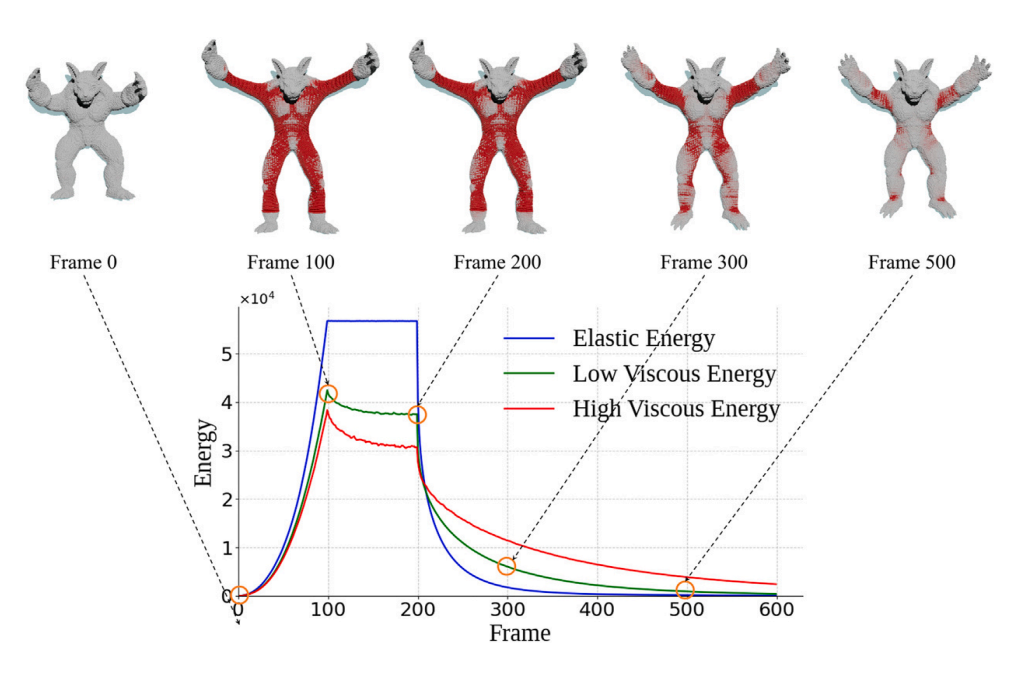


Fig. 5. Energy evolution of the armadillo stretching experiments.

material lies between the two. These results demonstrate the effectiveness of our viscoelastic model and its strong tunability in capturing diverse material responses.

To further evaluate the time-dependent behavior of the three materials, we perform a quantitative analysis of their creep and stress relaxation responses. As shown in Fig. 6(a), under a constant gravitational load, the elastic material exhibits continuous oscillations in strain due to inertia and elastic rebound. In contrast, the high-viscoelastic material shows a continuous increase in strain over time, eventually approaching a steady-state value. The low-viscoelastic material also undergoes time-dependent strain growth under the same load, albeit with a smaller magnitude. As illustrated in Fig. 6(b), during the interval from 0 to 0.75 s, the material is stretched at a constant rate, after which the strain remains fixed. In this constant-strain phase, the stress in the elastic material remains unchanged, indicating the absence of stress relaxation. In contrast, the stress in the high-viscoelastic material decreases significantly over time, demonstrating that internal viscous damping continuously dissipates energy, thereby reducing the stress required to sustain the same deformation.

Sand simulation: We designed a series of granular flow experiments and compared them with MPM simulations based on the Drucker–Prager yield criterion. These comparisons validate the effectiveness of different yield mapping schemes under the peridynamic framework in reproducing physically plausible granular flow and pile-up behaviors.

Fig. 7 shows a sand pile experiment with  $E_0 = 3 \times 10^5$  and  $\nu = 0.2$ . Under high friction coefficients, our method successfully produced stable, high-friction sandpiles in which the upper particles resisted sliding. Compared to the MPM approach under the same friction angle and coefficient, our method achieved more pronounced pile-up effects by introducing stronger cohesive forces. Additionally, the peridynamics framework, extended from elastic energy, allows for larger time steps, improving overall simulation efficiency.

To further study the influence of cohesion, we conducted a slope-divided sand pile experiment (Fig. 8). We used the Drucker–Prager yield criterion with  $E_0=2\times10^5$  and  $\nu=0.2$ , and used materials with different cohesion coefficients. Under higher cohesion, some sand particles could adhere to the inclined surface forming local accumulations. For lower cohesion, only a thin layer of particles remained, with the rest quickly sliding down. The accumulation patterns on the ground also showed significant differences: high-cohesion materials formed more compact sand pile structures; low-cohesion materials appeared more dispersed.

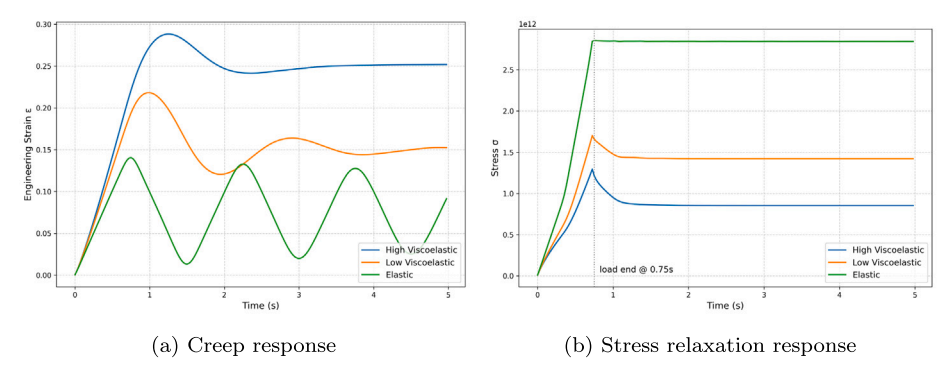
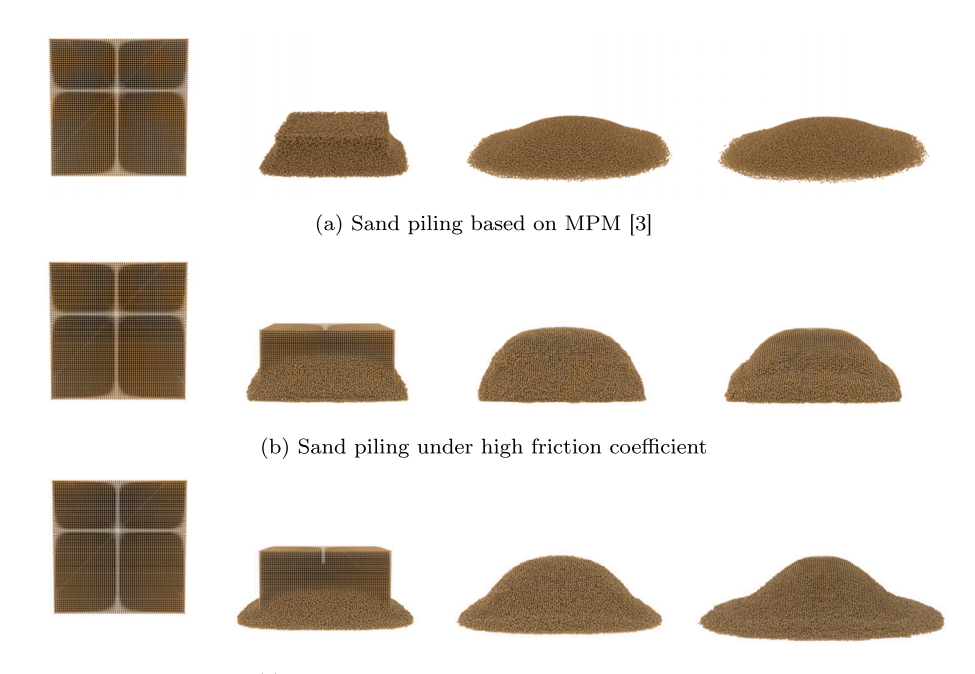
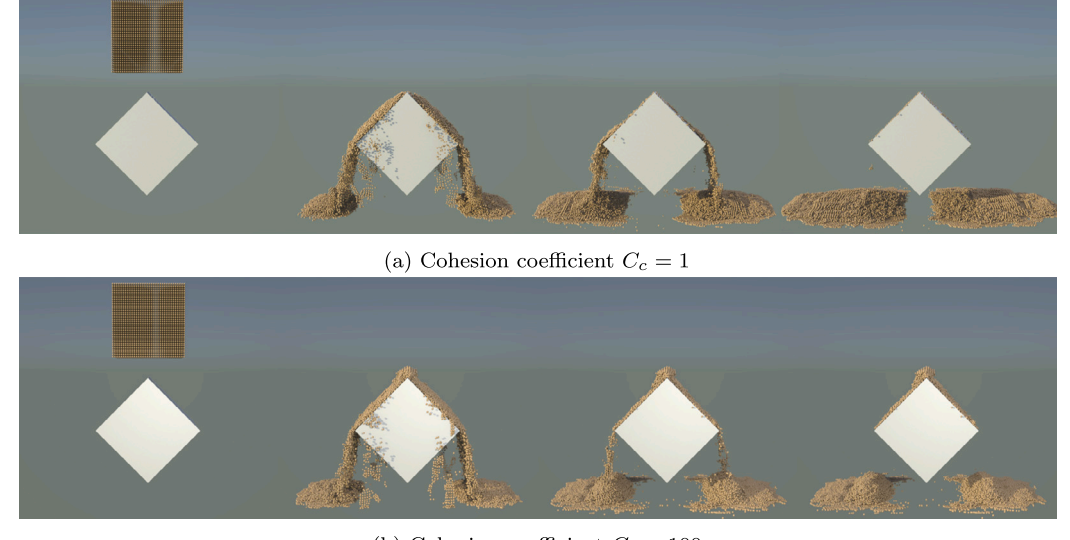


Fig. 6. Creep and stress relaxation behavior of elastic and viscoelastic materials.



 $(\mathbf{c})$  Sand piling under high cohesion coefficient

Fig. 7. Sand piling simulation experiments.



(b) Cohesion coefficient  $C_c = 100$ 

Fig. 8. Sand-slope experiments.

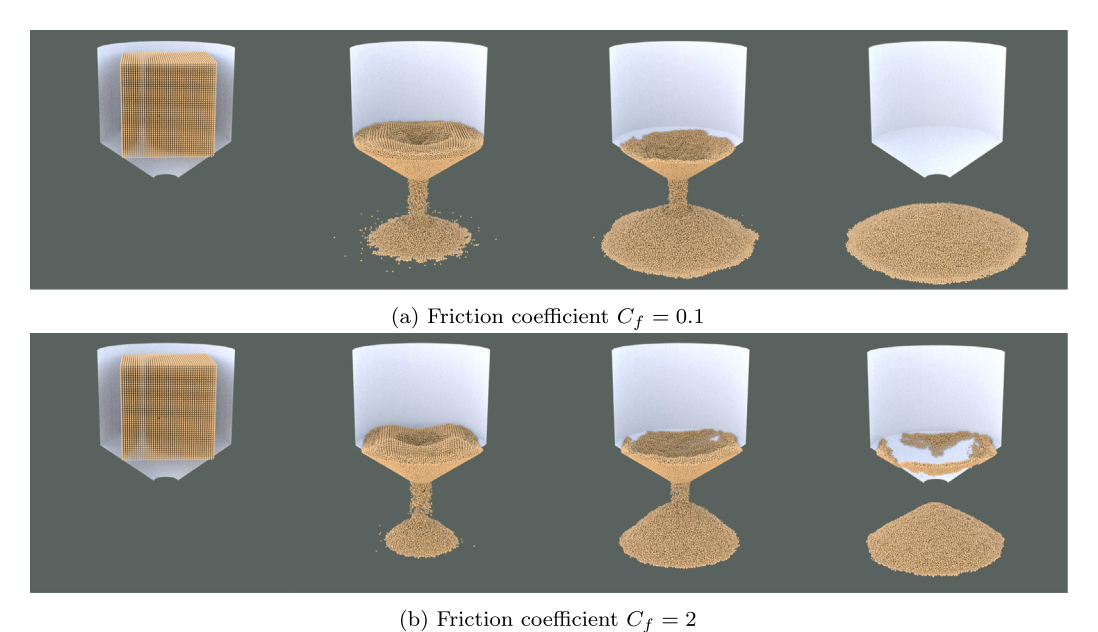
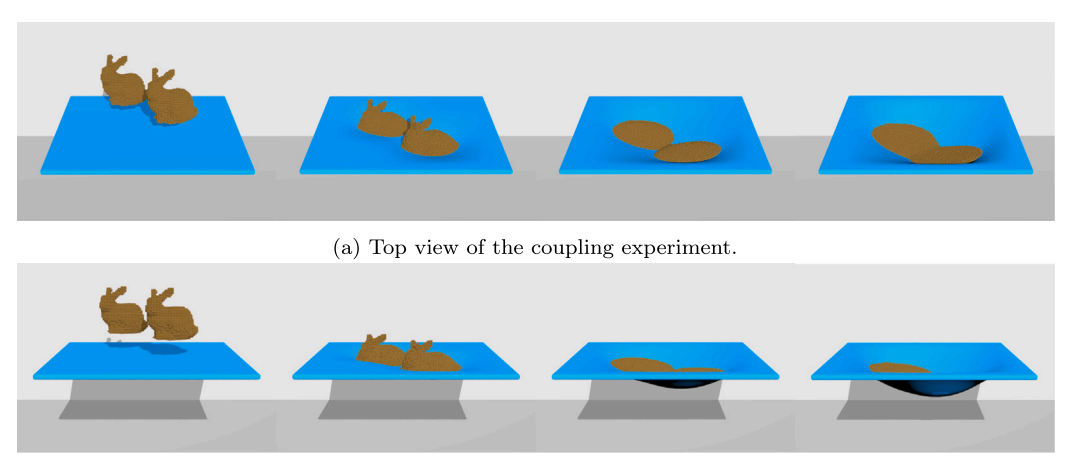


Fig. 9. Hourglass experiments.



(b) Side view of the coupling experiment.

Fig. 10. Elastic cloth and bunny-shaped sand coupling experiment.

To evaluate the influence of friction coefficients on granular flow behavior and accumulation patterns, we conducted an hourglass experiment under constant cohesion (Fig. 9). The results show that higher friction coefficients yield in poorer flow of particles near boundaries, while internal particles still show a certain flow. In contrast, materials with low friction exhibited more uniform flow between interior and exterior regions. After exiting the funnel, high-friction materials formed taller and steeper piles, while low-friction materials produced flatter deposits.

Coupling simulation: To evaluate the capability of our framework in simulating interactions between thin films and granular materials, we designed an experiment involving an elastic cloth and bunny-shaped sand (Fig. 10). The material parameters of the cloth are  $E_0 = 5 \times 10^7$ ,  $\nu = 0.45$ , while those of the sand are  $E_0 = 1 \times 10^5$ ,  $\nu = 0.2$ . During the experiment, the sand falls freely and accumulates on the cloth surface without penetration, while the cloth undergoes significant deformation under the coupled contact forces. The results demonstrate realistic twoway coupling, where both materials mutually influence each other's motion and deformation during collision and accumulation.

# 9. Conclusions and future work

We proposed a unified visco-elasto-plastic simulation framework based on SBPD to address the limitations of CCM in modeling discontinuities. Our framework demonstrates flexibility and effectiveness in simulating both viscoelastic solids and granular materials.

In terms of viscoelastic simulation, we derived time-dependent force density formulations based on the Prony model, accurately capturing complex response characteristics such as stress relaxation, creep, and hysteresis. For granular flow simulation, we integrated various yield criteria and mapping strategies, combined with density-based dynamic stiffness adjustment mechanisms, achieving natural flow, accumulation, and separation behaviors of particles. The framework further supports interactions among viscoelastic solids, granular media, and rigid bodies via a multi-material coupling mechanism, enhancing its robustness and applicability.

However, the computational efficiency of the current method for large-scale granular flow simulations still remains a challenge.

In future work, we will focus on developing implicit iterative acceleration strategies to enhance the stability and efficiency of large-scale computations. Furthermore, we plan to leverage the advantages of Peridynamics in handling fracture and crack propagation by incorporating fracture mechanics mechanisms into the viscoelastic model, enabling the simulation of richer material discontinuity behaviors. Building on the extensibility of our framework, we will also integrate viscoelastic fluids into the unified framework, extending its application capabilities in biological fluid and soft matter simulations.

#### CRediT authorship contribution statement

Jiamin Wang: Writing – original draft, Methodology, Code implementation. Haoping Wang: Data curation, Validation. Xiaokun Wang: Conceptualization. Yalan Zhang: Formal analysis. Jiří Kosinka: Writing – review & editing, Supervision. Steffen Frey: Writing – review & editing, Methodology. Alexandru Telea: Writing – review & editing, Supervision. Xiaojuan Ban: Project administration.

#### Declaration of competing interest

The authors declare that they have no known competing financial interests or personal relationships that could have appeared to influence the work reported in this paper.

## Acknowledgments

This work was supported by National Major Science and Technology Project of China (2024ZD0608100), Key Research and Development Program of Hainan Province (ZDYF2024GXJS032), Basic and Applied Basic Research Foundation of Guangdong Province (2023A1515030 177), National Natural Science Foundation of China (Nos. 62376025, 62332017), and China Scholarship Council (202306460015). The authors would also like to thank Dr. Cara Tursun for providing the workstation and NVIDIA GeForce RTX 4090 GPU used in this research.

#### Appendix A. Supplementary data

Supplementary material related to this article can be found online at https://doi.org/10.1016/j.cag.2025.104463.

# Data availability

Data will be made available on request.

## References

- [1] Viriyayuthakorn M, Caswell N. Finite element simulation of viscoelastic flow. J Non-Newton Fluid Mech 1980;6(3–4):245–67.
- [2] Romeo M, Monteagudo C, Sánchez-Quirós D. Muscle and fascia simulation with extended position based dynamics. Comput Graph Forum 2020;39(1):134–46.
- [3] Klár G, Gast T, Pradhana A, Fu C, Schroeder C, Jiang C, Teran J. Drucker-Prager elastoplasticity for sand animation. ACM TOG 2016;35(4):1–12.

- [4] Zhu K, He X, Li S, Wang H, Wang G. Shallow sand equations: real-time height field simulation of dry granular flows. IEEE Trans Vis Comput Graphics 2019;27(3):2073–84.
- [5] Stomakhin A, Schroeder C, Chai L, Teran J, Selle A. A material point method for snow simulation. ACM TOG 2013;32(4):1–10.
- [6] Gissler C, Henne A, Band S, Peer A, Teschner M. An implicit compressible SPH solver for snow simulation. ACM TOG 2020;39(4):36:1–36:16.
- [7] Tampubolon A, Gast T, Klár G, Fu C, Teran J, Jiang C, Museth J. Multi-species simulation of porous sand and water mixtures. ACM TOG 2017;36(4):1–11.
- [8] Gao M, Pradhana A, Han X, Guo Q, Kot G, Sifakis E, Jiang C. Animating fluid sediment mixture in particle-laden flows. ACM TOG 2018;37(4):1–11.
- [9] Silling S. Reformulation of elasticity theory for discontinuities and long-range forces. J Mech Phys Solids 2000;48(1):175–209.
- [10] Silling S, Epton M, Weckner O, Xu J, Askari E. Peridynamic states and constitutive modeling. J Elasticity 2007;88:151–84.
- [11] Lu Z, He X, Guo Y, Liu X, Wang H. Projective peridynamic modeling of hyperelastic membranes with contact. IEEE Trans Vis Comput Graphics 2023;30(8):4601–14.
- [12] Wang H, Wang X, Xu Y, Zhang Y, Yao C, Guo Y, Ban X. Peridynamic-based modeling of elastoplasticity and fracture dynamics. Comput Animat Virtual Worlds 2024;35(4):e2242.
- [13] Terzopoulos D, Platt J, Barr A, Fleischer K. Elastically deformable models. In: Proc. CGI. 1987, p. 205–14.
- [14] Terzopoulos D, Fleischer K. Modeling inelastic deformation: viscolelasticity, plasticity, fracture. In: Proc. CGI. 1988, p. 269–78.
- [15] Müller M, Charypar D, Gross M. Particle-based fluid simulation for interactive applications. In: Proc. SCA. 2003, p. 154–9.
- [16] Takahashi T, Dobashi Y, Fujishiro I, Nishita T, Lin M. Implicit formulation for SPH-based viscous fluids. Comput Graph Forum 2015;34(2):493–502.
- [17] Peer A, Gissler C, Band S, Teschner M. An implicit SPH formulation for incompressible linearly elastic solids. Comput Graph Forum 2018;37(6):135–48.
- [18] Tu Z, Li C, Zhao Z, Liu L, Wang C, Wang C, Qin H. A unified MPM framework supporting phase-field models and elastic-viscoplastic phase transition. ACM TOG 2024:43(2):1–19.
- [19] Yue Y, Smith B, Batty C, Zheng C, Grinspun E. Continuum foam: A material point method for shear-dependent flows. ACM TOG 2015;34(5):1–20.
- [20] Fang Y, Li M, Gao M, Jiang C. Silly rubber: an implicit material point method for simulating non-equilibrated viscoelastic and elastoplastic solids. ACM TOG 2019;38(4):1–13.
- [21] Bußler M, Diehl P, Pflüger D, Frey S, Sadlo F, Ertl T, Schweitzer MA. Visualization of fracture progression in peridynamics. Comput Graph 2017;67:45–57.
- [22] Madenci E, Oterkus S. Ordinary state-based peridynamics for thermoviscoelastic deformation. Eng Fract Mech 2017;175:31–45.
- [23] Ozdemir M, Oterkus S, Oterkus E, Amin I, El-Aassar A, Shawky H. Fracture simulation of viscoelastic membranes by ordinary state-based peridynamics. Proced Struct Integr 2022;41:333–42.
- [24] Zhu Y, Bridson R. Animating sand as a fluid. ACM TOG 2005;24(3):965-72.
- [25] Narain R, Golas A, Lin M. Free-flowing granular materials with two-way solid coupling. In: Proc. SIGGRAPH Asia. 2010, p. 1–10.
- [26] Lenaerts T, Dutré P. Mixing fluids and granular materials. In: Comp graph forum. Vol. 28, 2009, p. 213–8.
- [27] Daviet G, Bertails-Descoubes F. A semi-implicit material point method for the continuum simulation of granular materials. ACM TOG 2016;35(4):1–13.
- [28] Lai X, Ren B, Fan H, Li S, Wu C, Regueiro R, Liu L. Peridynamics simulations of geomaterial fragmentation by impulse loads. Int J Numer Anal Methods Geomech 2015;39(12):1304–30.
- [29] Simo JC, Hughes TJ. Computational inelasticity, vol. 7, Springer Science & Business Media; 2006.
- [30] He X, Wang H, Wu E. Projective peridynamics for modeling versatile elastoplastic materials. IEEE TVCG 2017;24(9):2589–99.